Physics in Medicine & Biology

IPEM Institute of Physics and Engineering in Medicine

PAPER

The impact of pencil beam scanning techniques on the effectiveness and efficiency of rescanning moving targets

To cite this article: G Klimpki *et al* 2018 *Phys. Med. Biol.* **63** 145006

IOP Publishing Phys. Med. Biol. 63 (2018) 145006 (13pp) https://doi.org/10.1088/1361-6560/aacd27

Physics in Medicine & Biology

IPEM Institute of Physics and Engineering in Medicine

PAPER

The impact of pencil beam scanning techniques on the effectiveness and efficiency of rescanning moving targets

G Klimpki[1], Y Zhang[1], G Fattori[1], S Psoroulas[1], D C Weber[1,2,3], A Lomax[1] and D Meer[1]

[1] Paul Scherrer Institute (PSI), Center for Proton Therapy, 5232 Villigen PSI, Switzerland
[2] Department of Radiation Oncology, University Hospital Zurich, Rämistrasse 100, 8091 Zurich, Switzerland
[3] Department of Radiation Oncology, University Hospital Bern, Freiburgstrasse 18, 3010 Bern, Switzerland

E-mail: grischa.klimpki@psi.ch

RECEIVED
22 December 2017

REVISED
3 June 2018

ACCEPTED FOR PUBLICATION
18 June 2018

PUBLISHED
11 July 2018

Keywords: pencil beam scanning, beam delivery, motion mitigation, rescanning, proton therapy

Supplementary material for this article is available online

Abstract

Therapeutic pencil beams are typically scanned using one of the following three techniques: spot scanning, raster scanning or line scanning. While providing similar dose distributions to the target, these three techniques can differ significantly in their delivery time sequence. Thus, we can expect differences in effectiveness and time efficiency when trying to mitigate interplay effects using rescanning. At the Paul Scherrer Institute, we are able to irradiate treatment plans using either of the three delivery techniques. Hence, we can compare them directly with identical underlying machine parameters such as energy switching time or minimum/maximum beam current. For this purpose, we selected three different liver targets, optimized plans for spots, and converted them to equivalent raster and line scanning plans.

In addition to the scanning technique, we varied the underlying motion curve, starting phase, prescription dose and rescanning strategy, which resulted in a total of 1584 4D dose calculations and 49 measurements. They indicate that rescanning becomes effective when achieving a high number of rescans for *every* dose element. Fixed minimum spot weights for spot and raster scanning machines often hamper this. By introducing adaptive scaling of the beam current within iso-energy layers for line scanning, we can flexibly lower the minimum weight whenever required and achieve higher rescanning capability. Averaged over all scenarios studied, volumetric rescanning is significantly more effective than layered provided the same number of rescans are applied. Fast lateral scanning contributes to the efficiency of rescanning. We observed that in any given time window, we can always perform more rescans using raster or line scanning compared to spot scanning irradiations. Thus, we conclude that line scanning represents a promising technique for rescanning by combining both effectiveness and efficiency.

1. Introduction

Particle therapy centers increasingly use the method of pencil beam scanning (PBS), as defined by Flanz (2011), to distribute dose in the tumor volume. Meer and Psoroulas (2015) showed that by the end of 2014, almost 50% of all particle therapy gantries around the world were equipped with PBS technology. In PBS, a pair of scanner magnets deflects the beam in the lateral plane. In addition, the beam energy can be modified to successively change the penetration depth of the beam. By alternating lateral scans and changes in energy, particles and their dose deposition can be distributed throughout the 3D tumor volume.

The beam scanning process in the lateral plane is typically performed in three different ways: using spot scanning, raster scanning or line scanning[4]. Spot scanning was introduced clinically by Pedroni *et al* (1995) at the Paul Scherrer Institute (PSI) and has also been adopted in the first-generation scanning system at the MD Anderson Cancer Center (Smith *et al* 2009) as well as at the Massachusetts General Hospital (Grassberger *et al* 2013). Raster

[4] Wobbling is not considered here as it requires patient-specific hardware such as collimators and compensators.

scanning, on the other hand, was first introduced by Haberer *et al* (1993) at the Gesellschaft für Schwerionenforschung (GSI). Many facilities treating with carbon ions, e.g. HIT in Germany (Haberer *et al* 2004), NIRS in Japan (Furukawa *et al* 2010b) and CNAO in Italy (Giordanengo *et al* 2015), make use of the raster scanning technique. Line scanning was introduced recently by PSI (Zenklusen *et al* 2010) and Sumitomo Heavy Industries, Ltd. (Inoue 2014) and is used clinically at Samsung Medical Center, Seoul, South Korea (Kwangzoo *et al* 2015). Spot and raster scanning systems are also offered by a number of industrial vendors (e.g. IBA, Hitachi or Varian).

These three scanning techniques may differ in performance, but they all exhibit increased sensitivity to periodic, intra-fractional motion (e.g. breathing, heartbeat, intestinal activity) compared to passive scattering irradiations. The reason for this is the motion of the patient anatomy that interferes with the motion of the particle beam. Resulting interference or so-called interplay patterns/effects—hot and cold spots in the delivered dose distribution—can be mitigated in various ways (Bert and Durante 2011). Rescanning is one of the investigated methods: the idea, suggested decades ago, is to irradiate the same field multiple times with proportionally reduced dose to blur out interplay patterns (Phillips *et al* 1992). This approach requires increased margins of the target that encompass its motion, but it imposes relatively low technical demands on the beam delivery system compared to e.g. tumor tracking (Riboldi *et al* 2012).

Published studies identify numerous factors that influence the effectiveness of rescanning such as motion amplitude (Bert *et al* 2008, Schätti *et al* 2013), motion estimation (Zhang *et al* 2012), beam width (Grassberger *et al* 2013), tumor size (Zenklusen *et al* 2010) or rescanning type (Bernatowicz *et al* 2013, Schätti *et al* 2013, Grassberger *et al* 2015). Furthermore, they reveal a strong dependence of the efficiency of rescanning on the beam delivery system (Furukawa *et al* 2010a, Schätti *et al* 2014) and the integration into the clinical workflow (Mori *et al* 2014a, 2014b). All these studies have in common that their findings are coupled to the underlying beam scanning technique. Even though Bernatowicz *et al* (2013) and Dowdell *et al* (2013) varied the characteristics of beam delivery for spot scanning in simulation studies, we still lack a comprehensive comparison of the three scanning techniques available and their impact on rescanning under identical irradiation conditions (same accelerator, dose rate, beam size etc). On the second-generation gantry at PSI, so-called Gantry 2, we have the unique opportunity to irradiate patient plans in either spot, raster or line scanning mode. Hence, we can directly compare these three techniques and their impact on rescanning under identical irradiation conditions.

For this purpose, we conducted a comparative study on the effectiveness and efficiency of spot, raster and line scanning to mitigate interplay effects using rescanning. We investigated three liver targets following two different (patient-specific) breathing curves. Furthermore, we varied the fraction dose, the starting phase as well as the type and the amount of rescans. By studying the impact of all these parameters on simulated and measured dose distributions, we wish to answer the following three questions:

- How do magnitudes of interplay patterns compare across the different scanning techniques?
- Which technique is most effective and which is most efficient when combined with rescanning?
- Does one of the three techniques exhibit superior combination of effectiveness and efficiency?

Within this study, we developed a treatment plan converter that translates plans optimized for spot scanning to raster and line scanning plans of similar quality. All plans are deliverable on Gantry 2, which, for experimental purposes, can perform irradiations in all three scanning modes.

2. Materials and methods

2.1. Beam delivery techniques

In *spot scanning*, lateral pencil beam positions are discretized on a rectilinear grid. For beams in anterior/posterior direction, the lateral (T, U)-plane coincides with the coronal plane of the patient. The number of protons delivered to every grid point (or spot) is simply given by the dwell time of the beam. Before switching from one spot to another, the beam is turned off completely, which results in roughly 3 ms dead time between spot transitions (value for PSI Gantry 2). The distance between grid points can, in principle, vary as function of beam energy. However, to be consistent with our clinical protocol, we selected fixed grid distances of $\Delta T = \Delta U = 4$ mm. *Raster scanning* follows the same rectilinear grid, but the beam remains on when moving from one grid point to the next. As such, raster scanning saves dead time at the cost of introducing small transient doses. When the distance between two prescribed beam positions exceeds an upper limit (here 10 mm), a beam-off command needs to be issued nonetheless. *Line scanning* is fully continuous in T-direction and not bound to any grid constraints in this dimension. The delivered dose can be modulated by changing the scan speed and beam current dynamically during irradiation. The beam is switched off only when changing U-position. Due to different control mechanisms in spot and line scanning, we expect an increased dead time between two lines of roughly 7.9 ms. Figure 1 exemplifies how the same iso-energy layer would be delivered in spot scanning (left), raster scanning (middle) and line scanning mode (right).

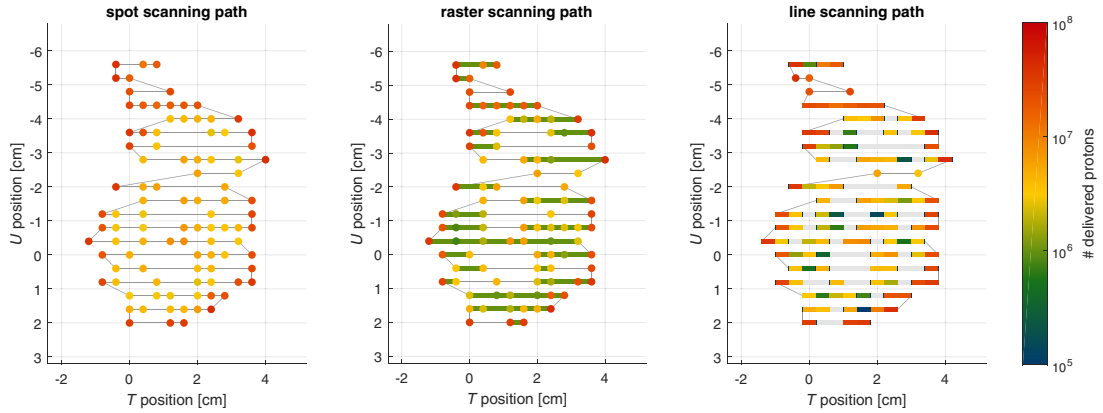

Figure 1. Scan paths for all three scanning techniques: spot scanning (left), raster scanning (middle) and line scanning (right). The three illustrations represent the same iso-energy slice ($E = 151$ MeV) of patient $\mathcal{P}_3$ (see table 1). Beam weights were optimized for a total field dose of 0.606 Gy.

Table 1. gITV sizes for all six combinations of 3D CT geometry and 4D MRI motion.

	motion data[a] $\mathcal{M}_1$: $\langle A_{pp}\rangle = (5.1 \pm 1.3)$ mm $\langle\tau\rangle = (3.2 \pm 0.3)$ s	motion data[a] $\mathcal{M}_2$: $\langle A_{pp}\rangle = (16.9 \pm 2.4)$ mm $\langle\tau\rangle = (6.6 \pm 0.8)$ s
patient data[b] $\mathcal{P}_1$: CTV of 95 cm^3	148 cm^3	184 cm^3
patient data[b] $\mathcal{P}_2$: CTV of 220 cm^3	313 cm^3	382 cm^3
patient data[b] $\mathcal{P}_3$: CTV of 340 cm^3	458 cm^3	528 cm^3

[a] obtained from 4D MRI;
[b] obtained from 3D CT.

2.2. Patient cases and treatment plans

The patient data set comprises 3D computed tomography scans (3D CTs) of liver tumors stemming from three different patients as well as 4D magnetic resonance imaging (4D MRI) under free breathing (Zhang *et al* 2016). The delineation of the clinical target volumes (CTVs) was based on the 3D CTs. From each 4D MRI, we extracted patient-specific motion vector fields over the entire period of image acquisition. To simulate target motion under breathing, we applied these vector fields to the static 3D CT using deformable image registration. This procedure was introduced and described in more detail by Boye *et al* (2013). Table 1 shows how we combined three 3D CTs and two 4D MRIs in this study. Fairly small density variations inside the liver facilitate purely geometric target expansion to encompass the full extent of the CTV motion (Knopf *et al* 2013). All treatment plans were optimized for homogeneous coverage of the resulting geometric internal target volumes (gITVs).

We chose a three-field arrangement for all six target volumes with conventional (2 Gy (RBE) per fraction) and hypo-fractionated irradiation scheme (6 Gy (RBE) per fraction). Each of the three fields was optimized for homogeneity separately (single-field uniform dose approach). Only the anterior-posterior field was considered in this comparison study (to limit the amount of variable parameters) and was prescribed doses of 0.606 Gy and 1.818 Gy, respectively. All plans were optimized for spot scanning on a (4×4) mm^2 rectilinear spot grid. Figure 2 shows static dose distributions at the center of the spread-out Bragg peak for all three patients included in this study. Raster and line scanning plans were created by converting the original spot scanning plan to the corresponding scanning technique (see section 2.4 below). A 3D re-optimization on the patient anatomy to account for the different delivery scenarios was not performed. Considering six different gITVs, two different field doses, and three different scanning techniques yields 36 static plans in total.

2.3. Rescanning strategy

To investigate the effectiveness of each scanning technique in mitigating tumor motion using rescanning, we split the field dose of every plan in 2, 4, 6, 8 and 10 scans (R_{nom}). However, we respected the smallest deliverable number of protons $N_{\text{p,min}}$ when scaling the dose by evaluating the possible number of rescans $\lfloor R_i \rfloor$ separately for every dose element[5] i as follows:

$$\lfloor R_i \rfloor = \min\left\{ \left\lfloor \frac{N_{\text{p},i}}{N_{\text{p,min}}} \right\rfloor, R_{\text{nom}} \right\}. \quad (1)$$

[5] In spot and raster scanning, discrete grid points represent individual dose elements. In line scanning, one entire line is considered to be one dose element.

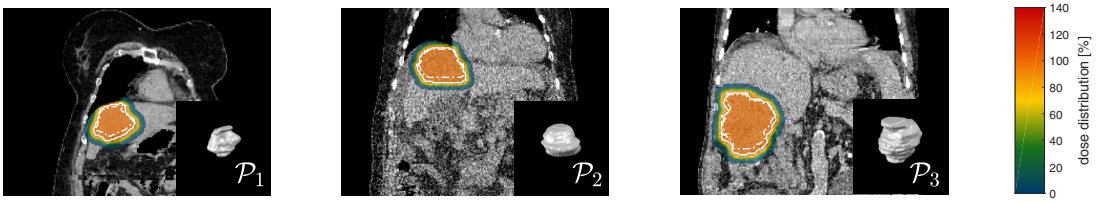

Figure 2. Static dose distributions for patients $\mathcal{P}_1$ (left), $\mathcal{P}_2$ (middle) and $\mathcal{P}_3$ (right). The CTV (dashed contour) was enlarged according to motion $\mathcal{M}_1$. All plans were optimized for spot scanning on the resulting gITV (solid contour). The insets show 3D renders of the CTV.

As such, not all dose elements with initial weight $N_{\mathrm{p},i}$ can receive the full number of anticipated rescans R_{nom}, with elements with very low initial weights being rescanned less than elements with high initial weights. During rescanning, we fill each iso-energy layer only with those elements that can actually receive a rescan. For spot and raster scanning, this can introduce gaps in the scan path, as observed in figure 1, meaning that some of the grid points may be empty. Zhang *et al* (2016) provide a more detailed description of this approach. In this study, we considered both layered and volumetric rescanning sequences as defined by Bert and Durante (2011).

2.4. Treatment plan conversion

In order to compare the different scanning techniques quantitatively, we developed a treatment plan converter that translates spot scanning plans to raster and line scanning plans. The converter respects all machine-related constraints such as maximum and minimum dose rate or maximum beam scanning speed and, thus, produces realistic and deliverable plans. In a first step, the converter groups all spots placed on straight lines (same U-position and same energy) and calculates their nominal fluence profile in water[6]. In case of raster scanning, transient dose contributions between spots are added and the original spot weights are decreased to preserve the total number of delivered protons. In case of line scanning, discrete beam spots are replaced by line segments scanned at constant speed and beam current. If a spot is located at position (T_j, U_j), the corresponding line segment will stretch from $(T_j - \Delta T/2, U_j)$ to $(T_j + \Delta T/2, U_j)$. To enable continuous motion of the beam in T-direction, ΔT resembles the grid distance of the original spot scanning plan (4 mm). In case of less than three spots per line, we keep the individual beam spots. Raster and line scanning fluence profiles obtained in this fashion deviate from the nominal spot scanning profile. Hence, we added an iterative matching step based on non-linear least squares that recalculates beam weights for all raster and line segments under the constraints of optimal fluence matching to those of the initial spot scanning plan.

To be compatible with most raster scanning installations, we assign a fixed beam current to every raster scanning path. Each path is interrupted only when changing U-position or if the change in T-position exceeds 10 mm (gap in the scan path). The former reason for interruptions is due to a limitation in our control system, the latter is common practice to prevent large transient doses. In line scanning, we allow for frequent modulation of the beam current during a single line. Hence, we can avoid interruptions due to gaps in the scan path by suppressing the beam current completely in those regions. The different handling of gaps in raster and line scanning mode can be seen in figure 1.

The maximum (minimum) point-to-point dose difference between translated raster and nominal spot scanning plans amounts to +2.7% (−2.4%) of the prescribed field dose. The considered voxel size measures 4.0 mm laterally and 2.5 mm in depth. The vast majority (95%) of all point-to-point dose differences inside the CTV is much smaller and ranges between +0.6% and −0.8% with a median difference of 0.0%. The agreement for line scanning is similar: the maximum (minimum) difference among all translated plans amounts to +1.8% (−2.1%) and the 95% interval spans from +0.9% and −0.4% (median difference 0.2%).

2.5. 4D dose calculation

We use time-resolved dose calculations to estimate the magnitude of dose deterioration due to motion of the anatomy during irradiation. Our dose calculation uses the motion vector field extracted from the 4D MRI to deform the dose calculation grid as function of time. Based on warped 3D CT information, water-equivalent path lengths and density information are adapted for every point in time. The anatomy, however, is assumed to be stationary during the irradiation of a single spot (∼few milliseconds duration). A full description of the algorithm was provided by Boye *et al* (2013). We recently validated it against measurements (Krieger *et al* 2018).

The 4D dose calculation was originally developed for spot scanning irradiations and supports input in form of spot lists only. Thus, we deconvolved raster and line scanning plans back to extended lists of discrete spots. To

[6] The width of the pencil beam for this calculation resembles the pencil beam width in water at the Bragg peak including both phase space and scattering contributions.

Table 2. Specifications of the Gantry 2 beam delivery system at the Paul Scherrer Institute (see supplementary material S1 for a detailed description (stacks.iop.org/PMB/63/145006/mmedia)).

	70 MeV	150 MeV	230 MeV
max. clinically used beam current[a, b] (pA)	65	400	514
min. clinically used beam current[a] (pA)	24	40	51
min. spot weight [10^5] for spot/raster scanning[a]	2.8	4.6	6.0
min. equiv. weight [10^5] for line scanning[c]	0.6	1.0	1.3
max. stable and reproducible scan speed in T-direction		1 cm ms^{-1}	
mean dead time between two spots		2.83 ms	
mean dead time between two lines		7.90 ms	
mean dead time between energy changed		106 ms	
mean ramping time of the beamline[d]		9.3 s	

[a] energy-dependent;
[b] transmission-dependent;
[c] distributed over 4 mm at maximum scan speed and minimum beam current;
[d] occurs when resetting all beamline elements between two volumetric rescans.

represent the dose deposition accurately, we decreased the spot grid in the T-direction down to 1 mm. In this way, we could mimic (quasi-)continuous irradiations and provide compatible input to our validated 4D dose calculation algorithm.

In addition to (extended) spot lists, the 4D dose calculation requires timestamps for every entry. These timestamps indicate how much time has passed between the overall start of the irradiation and the start of the current spot. To have precise estimates on relevant system delays and performance parameters, we analyzed machine log files from patient irradiations on Gantry 2 and derived a timing model. Input parameters to this model are listed in table 2. E.g. irradiating a single spot with 10^7 protons at 150 MeV requires

$$t_{\text{spot}} = 10^7 \times \frac{(1.602 \times 10^{-19}\,\text{C})}{(400 \times 10^{-12}\,\text{A})} \cong 4\,\text{ms} \tag{2}$$

with our maximum beam current (currently limited by radiation protection considerations). For each spot transition, we accumulate 2.83 ms of dead time on average. Hence, the next spot in the same energy layer will start 6.83 ms later. When changing the beam energy we have to account for another 106 ms dead time on average. Irradiations at low energies are affected by a drop in the beamline transmission[7] and, therefore, the irradiation time for every spot/line increases. Such effects are considered in our timing model and characterized through an energy-dependent look-up table. The total irradiation time t is given by the overall beam-on time and the sum of all dead times during the irradiation.

For all 36 static plans (six gITVs combined with two field doses and three scanning techniques), we calculated the corresponding 4D dose distributions on four different starting phases resulting in 144 non-compensated 4D dose calculations. Additionally, we calculated 4D dose distributions for each of the five rescanning numbers using both layered and volumetric sequences. Considering the same four starting phases as for the non-compensated calculations yields $36 \times 5 \times 2 \times 4 = 1440$ mitigated 4D dose calculations. In total, we end up with $144 + 1440 = 1584$ 4D and 36 static dose calculations on the corresponding 3D CTs.

2.6. Measurement devices and setup

Absolute dose distributions were measured with a 2D array of ionization chambers placed at iso-center (PTW *seven29*), whilst relative ones were measured with a scintillation screen coupled to a CCD camera (Schätti *et al* 2013). To be in agreement with our standard quality assurance workflow, we applied a constant output-scaling factor of 2% (Pedroni *et al* 2005) to all dose distributions measured with the PTW *seven29*. Both dosimeters could be moved with the QUASAR Respiratory Motion Platform during irradiation. It was programmed to reproduce patient-specific, rigid motions at the iso-center, as extracted from the 4D MRIs. All measurements were taken at 11 cm water-equivalent depth, which marks the center of the spread-out Bragg peak for patient $\mathcal{P}_3$. Krieger *et al* (2018) provide a more detailed description of the experimental setup.

[7] The transmission of the beamline is defined as the ratio of the beam current in the treatment room to the beam current extracted from the accelerator.

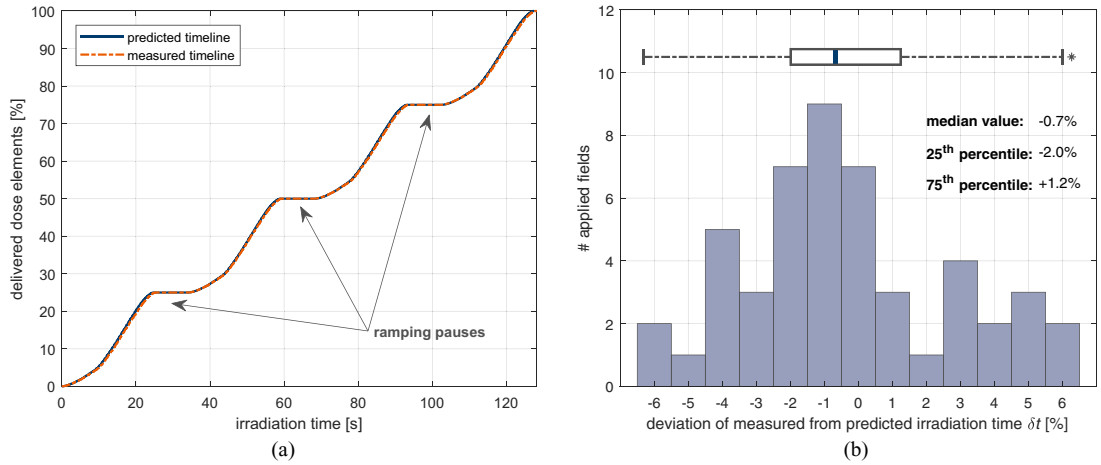

Figure 3. Deviations of the Gantry 2 timing model from actual machine performance for 49 irradiated fields (17 spot scans and 16 raster/line scans, respectively). (a) E.g. when rescanning patient $\mathcal{P}_3$ (1.818 Gy field) four times volumetrically using line scanning, the difference between measured and predicted irradiation time is below 1 s. This plot shows the result of one of the 49 irradiated fields. (b) 95% of all observed deviations are within −6.3% and +6.0%, with a median deviation of −0.7%.

2.7. Quantification metrics

We assessed the efficiency and effectiveness of spot, raster and line scanning based on the following three metrics:

(i) the total irradiation time t

(ii) the dose inhomogeneity $d_{5/95}$ defined as

$$d_{5/95} := \frac{D_{5\%} - D_{95\%}}{D_{\text{field}}}, \tag{3}$$

with the greatest dose $D_{5\%}$ which all but 5% of the CTV receives, the least dose $D_{95\%}$ received by at least 95% of the CTV and the prescribed field dose D_{field} (International Commission on Radiation Units and Measurements 2007)

(iii) the effective number of rescans R_{eff} defined as the average over all rescans per dose element $\lfloor R_i \rfloor$ (see equation (1))

3. Experiments and results

All absolute and relative dose measurements were conducted for patient $\mathcal{P}_3$ in combination with motion $\mathcal{M}_1$. We measured stationary and uncompensated dose distributions for each of the two field doses (0.6 Gy and 1.8 Gy) and each of the three scanning techniques ($2 \times 2 \times 3 = 12$ measurements). For the 1.8 Gy field, we additionally measured mitigated dose distributions for all of the five rescanning factors in both layered and volumetric rescanning sequences. We performed these measurements separately for each of the three scanning techniques ($5 \times 2 \times 3 = 30$ measurements). For the 0.6 Gy field, we randomly selected another seven rescanning cases resulting in a total of 49 irradiations. Based on these measurements, we validated the timing model of the machine, the treatment plan converter as well as the 4D dose calculation engine for the different beam scanning techniques (sections 3.1–3.3). The results of the 4D dose calculations are provided in section 3.4. A final experimental validation of the effectiveness and efficiency of rescanning can be found in section 3.5.

3.1. Experimental validation of the timing model

The Gantry 2 timing model, as described in section 2.5, is used as input to the 4D dose calculation algorithm. To have accurate estimates of the resulting interplay pattern, the timing model has to match the performance of the machine for all three scanning techniques. We validated our model against 49 irradiations on Gantry 2. 17 of those were carried out in spot scanning mode and 16 in raster and line scanning mode, respectively. We used the default machine log files to reconstruct the actual irradiation sequence and delivery timestamps (see figure 3(a)). The deviations of predicted and measured irradiation time for all scanning techniques are shown in figure 3(b). We see that 95% of all observed deviations are within −6.3% and +6.0%, with a median deviation of −0.7%.

3.2. Experimental validation of the plan converter

To demonstrate validity of the plan converter, we selected patient $\mathcal{P}_3$ and recalculated the dose distribution of the 1.818 Gy spot scanning field in water (see figure 4(a)). We defined 11 cm as reference depth, since it marks the

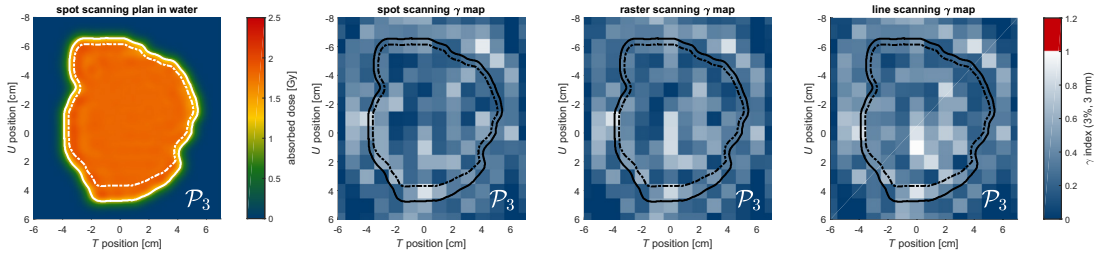

Figure 4. (a) Recalculated spot scanning plan of patient $\mathcal{P}_3$ in 11 cm water depth (1.818 Gy field). (b) γ-maps of the spot (left), raster (middle), and line scanning measurement (right) with respect to the recalculated spot scanning plan. The overall pass rate is at 100% in all cases. The dashed line represents the CTV contour and the solid line represents the gITV contour.

center of the spread-out Bragg peak. Using the PTW array, we measured absolute dose distributions at a water depth of 11 cm for raster and line scanning irradiations of the same field under static conditions. To compare measured dose distributions to the plan reference, we applied the γ-method introduced by Low *et al* (1998) with a distance-to-agreement of 3 mm and a dose-to-agreement of 3%. The resulting maps are shown in figure 4(b). We observe that all irradiations pass the criteria with 100%.

3.3. Experimental validation of the 4D dose calculation engine

Although we recently validated our 4D dose calculation algorithm for spot scanning irradiations (Krieger *et al* 2018), we wished to confirm the temporal validity of the dose calculation engine for raster and line irradiations, since these two scanning techniques comprise continuous movements of the proton beam. For this purpose, we acquired relative dose distributions in 11 cm water-equivalent depth with a CCD camera placed on a moving platform (see section 2.6 for a detailed description of the setup). We irradiated the 1.818 Gy field of patient $\mathcal{P}_3$ under motion $\mathcal{M}_1$ in all three delivery modes (no rescanning applied). The start of the irradiation was precisely synchronized to the start of the breathing curve using optical tracking of the motion platform (Fattori *et al* 2017). Figure 5(a) shows the measured interplay patterns, which differ across the different scanning techniques. Using machine and motion log files as well as quenching-corrected Bragg curves, we calculated the expected dose distributions using our 4D dose calculation engine (see figure 5(b)). All γ-maps between measured and calculated interplay patterns pass the $(3\% \mid 3\,\mathrm{mm})$-criterion with over 99%.

3.4. Results of the 4D dose calculations

In order to study the effectiveness and efficiency of the different scanning techniques for motion mitigation using rescanning, we have analyzed the results of all 1584 4D dose calculations using the metrics described in section 2.7. In particular, we considered the influence of the effective number of rescans R_{eff} and the influence of the rescanning sequence (layered versus volumetric) on effectiveness as well as the influence of the scanning technique (spot versus raster versus line scanning) on efficiency.

3.4.1. Effectiveness of rescanning.

We consider rescanning effective if it decreases inhomogeneities inside the target to close to the level of the static treatment plan ($d_{5/95} \sim 5\%$ for all targets). To quantify inhomogeneities, we calculated the $d_{5/95}$ inside the CTV as defined in equation (3) for all 4D dose calculations. The results for volumetric rescanning are shown in figure 6. We observe a decrease in inhomogeneity with increasing effective number of rescans R_{eff}. For motion $\mathcal{M}_1$ ($\mathcal{M}_2$), the median $d_{5/95}$ decreases from 22.43% (32.96%) for $R_{\mathrm{eff}} = 1$ to 7.38% (8.73%) for $R_{\mathrm{eff}} = 10$. Based on an analysis of variance, this trend is significant with $p \ll 10^{-10}$ for both motion cases. The scanning technique, starting phase, target size and field dose do not have a significant influence on the effectiveness of rescanning ($p > 0.1$). They contribute to the high fluctuations between the individual cases. For layered rescanning, we observed a less pronounced decrease in inhomogeneity with increasing R_{eff} (data not shown here).

In figure 7, we have plotted the $d_{5/95}$ of both rescanning sequences against each other. Each point in the graph represents one combination of scanning technique, starting phase, field dose, target size and effective number of rescans. We observe that the density distributions of the point clouds are shifted away from the line of iso-inhomogeneity indicating larger target inhomogeneities when rescanning layer-wise. The differences between the layered and volumetric approach are significant with p-values below 10^{-10}. This observation holds for both motion scenarios $\mathcal{M}_1$ and $\mathcal{M}_2$.

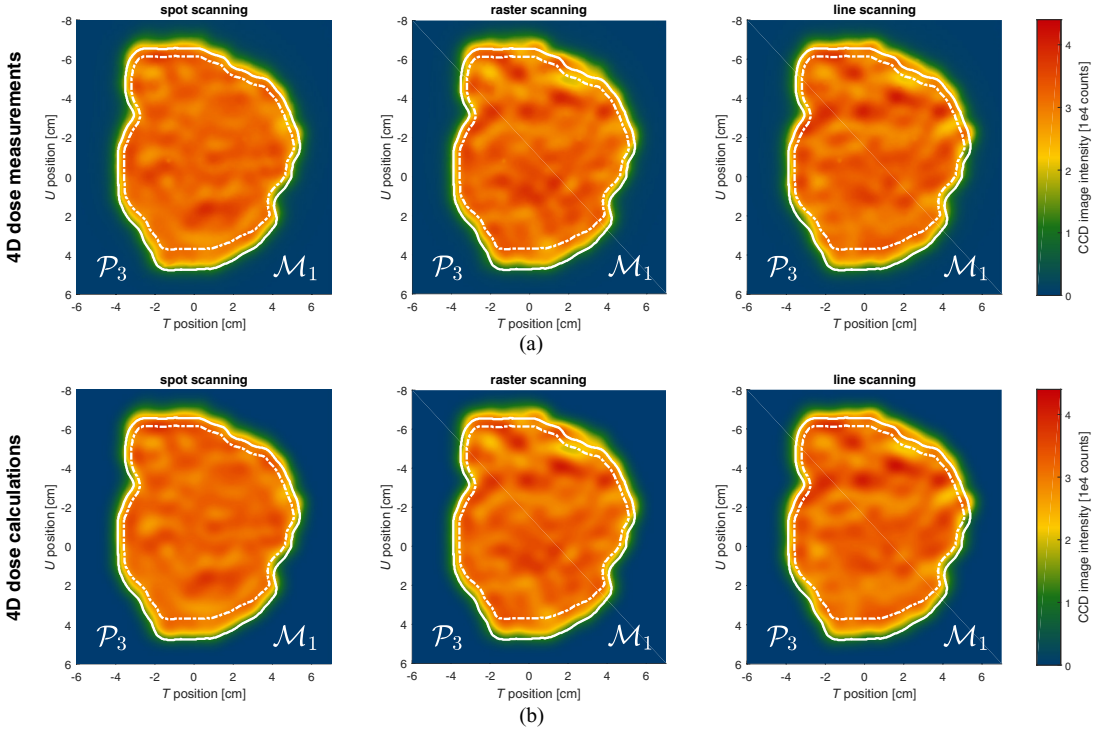

Figure 5. Comparison of measured (a) and calculated (b) interplay patterns for spot, raster and line scanning. We irradiated the 1.818 Gy field of patient $\mathcal{P}_3$ under motion $\mathcal{M}_1$ to a moving CCD camera. The 4D dose calculation, which was based on machine and motion log files as well as quenching-corrected Bragg curves, agrees with the measurement. The dashed line represents the CTV contour and the solid line represents the gITV contour.

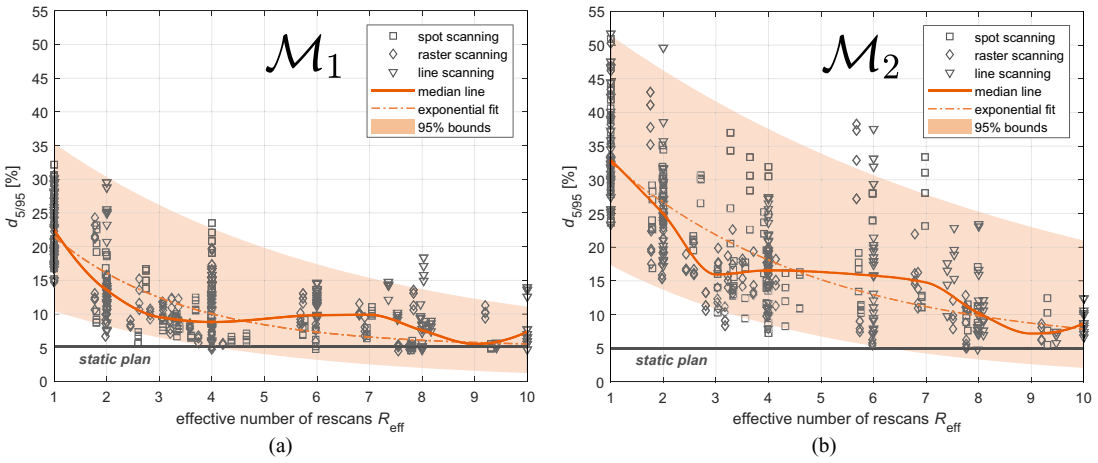

Figure 6. Target inhomogeneity $d_{5/95}$ of all 4D dose calculations concerning volumetric rescanning as a function of effective number of rescans R_{eff}. The results for motion $\mathcal{M}_1$ are shown in (a) and the results for motion $\mathcal{M}_2$ in (b). A high R_{eff} decreases target inhomogeneities significantly ($p \ll 10^{-10}$), whereas the scanning technique does not seem to influence the effectiveness of rescanning. The exponential bounds contain 95% of all data points and the solid curve indicates the median distribution.

3.4.2. *Efficiency of rescanning.*

In the previous section we showed that a high R_{eff} is needed in order to decrease inhomogeneities inside the target. But increasing the number of rescans will also increase the total irradiation time, making rescanning inefficient. In other words, we observe a trade-off between effectiveness and efficiency. Figure 8 shows that the sweet spot shifts across the different scanning techniques. Line scanning represents the fastest technique and has the ability to reach high rescanning numbers in shorter time windows. We also see that spot and raster scanning show difficulties in reaching high R_{eff} values: they are limited to 6.4 effective rescans for the 0.606 Gy field of patient $\mathcal{P}_3$, whereas line scanning can reach 12.8 effective rescans at maximum in this case. Last but not least, we observe that, despite being less effective for any given R_{eff}, layered rescanning is significantly faster than volumetric rescanning in all cases.

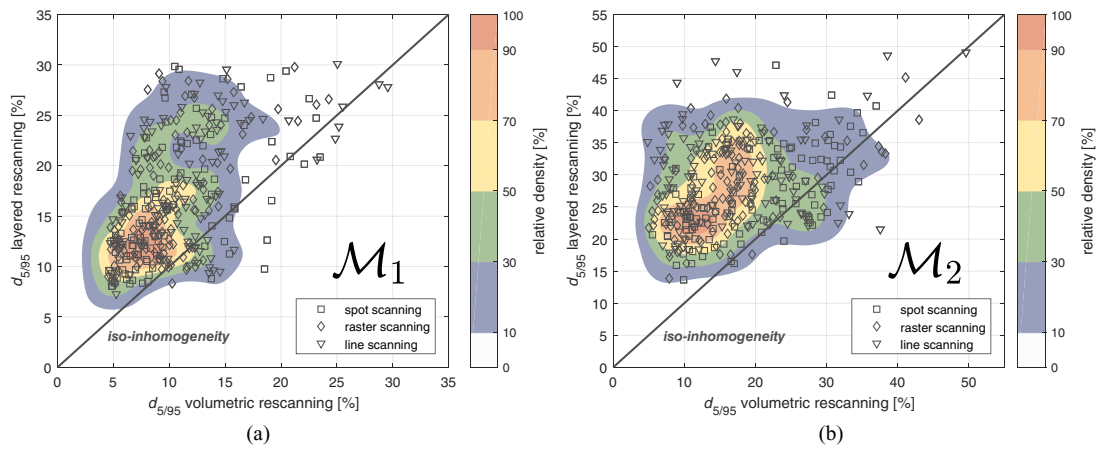

Figure 7. Target inhomogeneities $d_{5/95}$ of layered versus volumetric rescanning for motion $\mathcal{M}_1$ (a) and $\mathcal{M}_2$ (b). Data of all 4D dose calculations are shown in the two plots. The density of the point cloud is visualized in form of a color wash. We observe significantly higher inhomogeneities when rescanning layer-wise for both motion cases independent of the beam scanning technique.

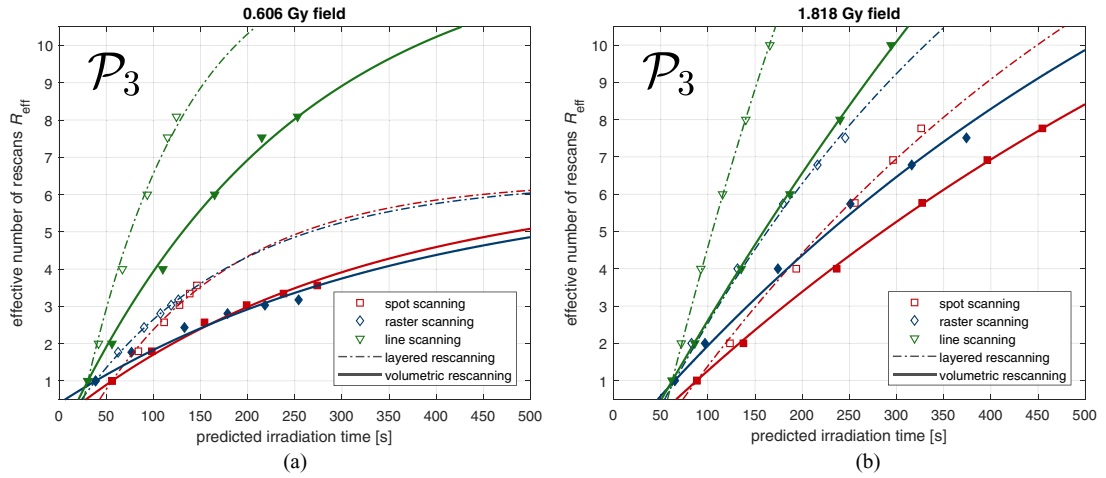

Figure 8. Effective number of rescans R_{eff} as a function of the predicted irradiation time for the low dose (a) and the high dose field (b) of patient $\mathcal{P}_3$. Layered rescanning is shown in dashed lines and volumetric rescanning in solid lines. Since $\mathcal{P}_3$ exhibits the largest gITV, differences in the irradiation times are most pronounced for this case.

3.5. Experimental validation of effectiveness and efficiency

To confirm the efficacy of all scanning techniques experimentally, we irradiated the 1.818 Gy field of patient $\mathcal{P}_3$ to a CCD camera following the motion curve $\mathcal{M}_1$. All dose distributions were measured in 11 cm water depth, which marks the center of the spread-out Bragg peak. We computed the $d_{5/95}$ inside the 2D CTV contour shown in figure 5(a) and compared it to the value of the static irradiation (CCD camera at rest) in figure 9(a)[8]. We can confirm that rescanning—in this case layer-wise—is effective, when reaching high values for R_{eff}. The overlapping confidence bounds of the exponential fits indicate that this observation is independent of the scanning technique. In this example case, spot scanning produces less interplay patterns in the unmitigated irradiation ($R_{\text{eff}} = 1$) than raster or line scanning. Note that the spot scanning irradiation for $R_{\text{eff}} = 1$ takes ∼25 s longer than the corresponding raster and line scanning irradiations, which allows for dose blurring over additional ∼8 motion periods (see table 1).

If we impose a constraint on the total irradiation time t, we will not be able to deliver the same number of rescans with all three scanning techniques because of varying efficiency. As such, we chose to restrict t to twice the time it takes to deliver the static spot scanning plan (160 s) and compare the measured inhomogeneities in figure 9(b). For this delivery time, layered rescanning is the most effective scenario for raster and line scanning, due to its faster delivery time and the higher R_{eff} that can be achieved within this time restriction. For spot scanning, two layered and two volumetric rescans yield similar mitigation strength with the latter being slightly more effective. With line scanning, we can reach the highest numbers of effective rescans, which reduces the $d_{5/95}$

[8] The absolute $d_{5/95}$ values of measurement and calculation should not be compared as the former represents one distinct layer in water whereas the latter stands for the entire CTV in patient anatomy.

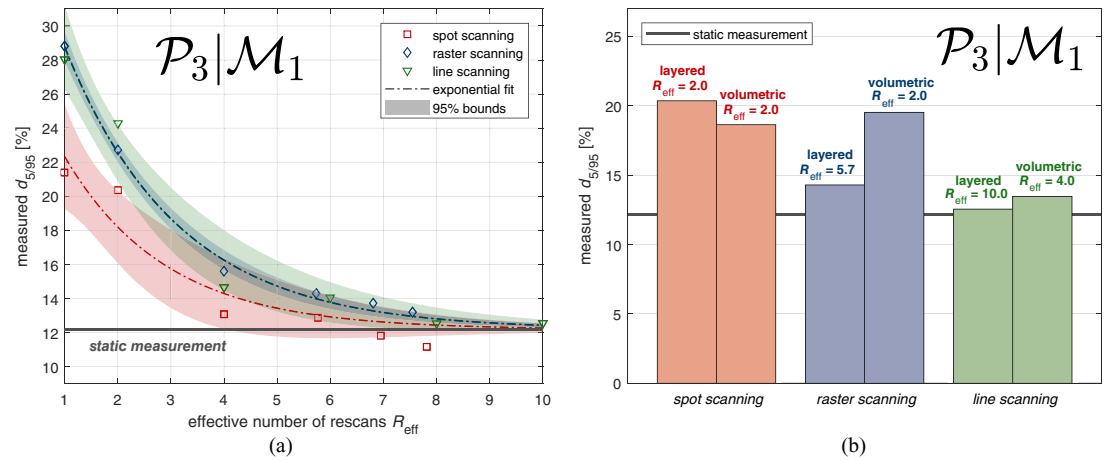

Figure 9. Experimental validation of effectiveness (a) and efficiency (b) of rescanning based on measurements for the 1.818 Gy field of patient $\mathcal{P}_3$ in combination with motion $\mathcal{M}_1$. (a) The measured target inhomogeneity $d_{5/95}$ decreases as function of R_{eff} for all scanning techniques. We considered layered rescanning in this example. (b) In a fixed time window (here 160 s), line scanning (green bars) can deliver more effective rescans than spot (red bars) or raster scanning (blue bars), which helps to decrease target inhomogeneity.

almost to the value of the static measurement. With raster scanning, we would be able to deliver 5.7 effective rescans (layer-wise) which yields a similar strength in mitigation. The efficiency of spot scanning and volumetric raster scanning is not high enough to effectively mitigate for interplay effects in this example.

4. Discussion and outlook

We found that rescanning can be an effective tool for motion mitigation when repeatedly irradiating the *entire* tumor volume. All dose elements of the plan should be visited multiple times, since a high effective number of rescans is key to successful mitigation. However, not all scanning techniques facilitate applying dose elements with very low weight, which limits their rescanning capability. Line scanning—with its combined speed and intensity modulation—shows the greatest flexibility in this regard. We also observed that maximizing the effective number of rescans comes at the cost of increasing the total irradiation time. As such, rescanning appears to be most efficient when applied using the line scanning technique.

We observed a significant correlation between decrease in target inhomogeneity ($d_{5/95}$) and increase in effective number of rescans (R_{eff}) that is independent of the applied scanning technique. While this correlation generally holds for both motion curves studied, we found a much larger spread in the data points calculated for the larger motion extent (see figure 6). This observation could indicate that rescanning alone may not be effective for tumors that move with peak-to-peak amplitudes of the order of ~15 mm or more. These findings are in agreement with previous works (Schätti *et al* 2013, Schätti *et al* 2014, Zhang *et al* 2016). Rescanning in combination with beam gating could be a viable approach in such cases. We should also note that dose inhomogeneity inside the target appears to be very case specific with rather high fluctuations for identical values of R_{eff}. Grassberger *et al* (2015) also conclude that it is difficult to predict the number of rescans required for individual patients. Hence, individual 4D dose calculations and interplay analyses are encouraged prior to patient treatment. The inhomogeneity caused by motion $\mathcal{M}_2$ is very large as indicated by the 4D dose calculations (see figure 6(b)). Thus, we decided to restrict all measurements to motion $\mathcal{M}_1$, where we see a clinically meaningful application of rescanning alone.

The total irradiation time is another important factor that influences the effectiveness of mitigation. Averaging out interplay patterns over many breathing cycles may help to lower the $d_{5/95}$ (Zenklusen *et al* 2010). This effect is certainly coupled to two of the main observations: (1) rescanning with a high R_{eff} is more effective than with a low one (see figure 6) and (2) volumetric rescanning is more effective than layered (see figure 7). In both cases, the more effective method exhibits a longer irradiation time. However, increased irradiation time alone cannot be the sole explanation for increased effectiveness as shown in figure 9(b). We see that, although having similar irradiation times, treatments with different R_{eff} and different rescanning sequences can indeed lead to varying $d_{5/95}$ values. Bernatowicz *et al* (2013) and Schätti *et al* (2013) came to similar conclusions.

Efficient rescanning requires fast lateral scanning (Grassberger *et al* 2015), as provided by raster and line scanning, as well as fast energy changes when irradiating in volumetric sequences (Bernatowicz *et al* 2013). On top of that, it necessitates a low minimum weight on applicable dose elements to ensure a high number of effective rescans. As such, adaptive scaling of the beam current at any given point in the target provides an advantage

(see table 2). In line scanning, we can regulate the current down to ∼10% of its maximum value within less than 100 μs. This allows for adapting irradiation settings locally rather than having the need to fix them globally: many commercially available systems set the beam current for an entire iso-energy layer based on the lowest-weighted element contained in that layer. Such constraints impair the efficiency of rescanning significantly (see figure 8). Spot or raster scanning combined with adaptive beam current scaling could, in principle, reach the same R_{eff} values as line scanning. For spot scanning, however, this approach would come at the cost of a dramatically increased delivery time due to the accumulation of dead time. Section S2 of the supplementary material describes the characteristics and limitations of beam current modulation on Gantry 2 in more detail.

In figure 7 we see, that volumetric rescanning is significantly more effective than layered rescanning. For the vast majority of data points—each representing one combination of target size, motion curve, starting phase, field dose and scanning technique—volumetric rescanning decreases target inhomogeneities further than layered. Several other studies support this result (Seco *et al* 2009, Schätti *et al* 2013, Zhang *et al* 2016). On the contrary, Bernatowicz *et al* (2013) and Grassberger *et al* (2015) concluded an increased sensitivity of volumetric rescanning to so-called synchronization or resonance effects. It is worth mentioning that both of them used periodically repeated motion curves, which may trigger or, at least, enhance this observation. By using irregular, patient-specific motion curves that have been recorded for >70 s (Zhang *et al* 2016), we hope to obtain more realistic estimates on the effectiveness of rescanning.

We acknowledge that the parameter space investigated in this study is limited to three patients and two motion characteristics. We chose to base our analysis upon patients with liver tumors, because the experimental plan converter yields best results for fairly homogeneous targets. In such cases, the prerequisites for plan conversion are optimal: spots are placed on (mostly) uninterrupted lines and their weights change rather gradually. Hence, by limiting this study to liver targets, we could rule out bias originating from differences in the initial plans, but we also lack information on the influence of density heterogeneities in the beam path (e.g. as for lung tumors). Furthermore, we restricted all measurements to irradiations of a non-deformable target. Validation of 4D dose calculations based on such measurements may be eligible when considering fairly homogeneous targets, but may require additional tests in case of density heterogeneities. Nonetheless, the measurements helped to gain trust and confidence in our 4D dose calculation algorithm as they confirm the results derived from the calculations.

In our current implementation, we begin the treatment of any patient with a ramping scheme that clears the history of all magnets on the gantry (∼10 s duration). Afterwards, we start the irradiation with the highest energy in the plan and lower it successively. Between two volumetric rescans, we have to repeat this ramping scheme, which makes it much slower than layered rescanning despite having short energy switching times (∼100 ms). By supporting successive upscaling of the energy in the control system, we could avoid these ramping pauses and e.g. decrease the irradiation time in figure 3(b) from ∼2 min to ∼$1\frac{1}{2}$ min. As such, the difference in efficiency between layered and volumetric rescanning would be minimized. Hence, we are currently implementing this variant of volumetric rescanning and plan to combine it with line scanning for patient treatments soon. Given that energy layer switching times for most commercial systems are much longer than those used in this work, especially for synchrotron-based facilities, we would hope that our efforts towards fast energy changes encourage manufacturers to pursue decreasing their energy layer switching times to facilitate volumetric rescanning.

5. Conclusions

Different pencil beam scanning techniques such as spot, raster or line scanning produce interplay patterns of comparable magnitude when irradiating moving targets. Motion mitigation using rescanning is most effective when achieving a high number of rescans for every dose element in the plan. While this observation is independent of the beam scanning technique, not all variants may be able to reach a high effective number of rescans due to technical constraints (e.g. lowest deliverable spot weight). In line scanning, we can adapt the beam current locally which facilitates delivery of very low doses with minimal compromise on the total irradiation time. Hence, we consider it an effective and efficient irradiation technique for rescanning.

Acknowledgments

The authors wish to thank the Massachusetts General Hospital for providing 3D CT data. Furthermore, they would like to express their gratitude to the Giuliana and Giorgio Stefanini Foundation for supporting this project. They declare they have no competing financial interests.

Author's contributions

GK performed experiments, analyzed the data and wrote the manuscript. YZ provided motion data, optimized treatment plans and calculated 4D dose distributions. GF supported execution of the measurements and provided optical tracking functionality. All authors commented on the paper and approved its final form.

ORCID iDs

G Klimpki https://orcid.org/0000-0001-7646-6200
Y Zhang https://orcid.org/0000-0003-1608-4467
G Fattori https://orcid.org/0000-0002-7639-7759

References

Bernatowicz K, Lomax A and Knopf A 2013 Comparative study of layered and volumetric rescanning for different scanning speeds of proton beam in liver patients *Phys. Med. Biol.* **58** 7905–20
Bert C and Durante M 2011 Motion in radiotherapy: particle therapy *Phys. Med. Biol.* **56** R113–44
Bert C, Grözinger S and Rietzel E 2008 Quantification of interplay effects of scanned particle beams and moving targets *Phys. Med. Biol.* **53** 2253–65
Boye D, Lomax T and Knopf A 2013 Mapping motion from 4D-MRI to 3D-CT for use in 4D dose calculations: a technical feasibility study *Med. Phys.* **40** 061702
Dowdell S, Grassberger C, Sharp G and Paganetti H 2013 Interplay effects in proton scanning for lung: a 4D Monte Carlo study assessing the impact of tumor and beam delivery parameters *Phys. Med. Biol.* **58** 4137–56
Fattori G, Safai S, Carmona Fernández P, Peroni M, Perrin R, Weber D and Lomax A 2017 Monitoring of breathing motion in image-guided PBS proton therapy: comparative analysis of optical and electromagnetic technologies *Radiat. Oncol.* **12** 63–74
Flanz J 2011 Particle beam scanning *Proton Therapy Physics* ed H Paganetti (Boca Raton, FL: CRC Press) pp 157–90
Furukawa T, Inaniwa T, Sato S, Shirai T, Mori S M, Takeshita E, Mizushima K, Himukai T and Noda K 2010a Moving target irradiation with fast rescanning and gating in particle therapy *Med. Phys.* **37** 4874–9
Furukawa T *et al* 2010b Performance of the NIRS fast scanning system for heavy-ion radiotherapy *Med. Phys.* **37** 5672–82
Giordanengo S *et al* 2015 The CNAO dose delivery system for modulated scanning ion beam radiotherapy *Med. Phys.* **42** 263–75
Grassberger C, Dowdell S, Lomax A, Sharp G, Shackleford J, Choi N, Willers H and Paganetti H 2013 Motion interplay as a function of patient parameters and spot size in spot scanning proton therapy for lung cancer *Int. J. Radiat. Oncol. Biol. Phys.* **86** 380–6
Grassberger C, Dowdell S, Sharp G and Paganetti H 2015 Motion mitigation for lung cancer patients treated with active scanning proton therapy *Med. Phys.* **42** 2462–9
Haberer T, Becher W, Schardt D and Kraft G 1993 Magnetic scanning system for heavy ion therapy *Nucl. Instrum. Methods Phys. Res.* A **330** 296–305
Haberer T, Debus J, Eickhoff H, Jäkel O, Schulz-Ertner D and Weber U 2004 The Heidelberg ion therapy center *Radiother. Oncol.* **73** S186–90
Inoue J 2014 Line scanning apparatus utilizing irradiation position and stationary time for scanning control *US Patent* no. 8890090
International Commission on Radiation Units and Measurements 2007 Prescribing, recording, and reporting proton-beam therapy—ICRU Report 78 *J. ICRU* **7** 29–48
Knopf A C, Boye D, Lomax A and Mori S 2013 Adequate margin definition for scanned particle therapy in the incidence of intrafractional motion *Phys. Med. Biol.* **58** 6079–94
Krieger M, Klimpki G, Fattori G, Hrbacek J, Oxley D, Safai S, Weber D, Lomax A and Zhang Z 2018 Experimental validation of a deforming grid 4D dose calculation for PBS proton therapy *Phys. Med. Biol.* **63** 055005
Kwangzoo C *et al* 2015 The first private-hospital based proton therapy center in Korea; status of the Proton Therapy Center at Samsung Medical Center *Radiat. Oncol. J.* **33** 337–43
Low D, Harms W, Mutic S and Purdy J 1998 A technique for the quantitative evaluation of dose distributions *Med. Phys.* **25** 656–61
Meer D and Psoroulas S 2015 Gantries and dose delivery systems *Mod. Phys. Lett.* A **30** 1540021
Mori S, Inaniwa T, Furukawa T, Takahashi W, Nakajima M, Shirai T, Noda K, Yasuda S and Yamamoto N 2014a Amplitude-based gated phase-controlled rescanning in carbon-ion scanning beam treatment planning under irregular breathing conditions using lung and liver 4DCTs *J. Radiat. Res.* **55** 948–58
Mori S, Zenklusen S, Inaniwa T, Furukawa T, Imada H, Shirai T, Noda K and Yasuda S 2014b Conformity and robustness of gated rescanned carbon ion pencil beam scanning of liver tumors at NIRS *Radiother. Oncol.* **111** 431–6
Pedroni E *et al* 1995 The 200 MeV proton therapy project at the Paul Scherrer Institute: conceptual design and practical realization *Med. Phys.* **22** 37–53
Pedroni E, Scheib S, Böhringer T, Coray A, Grossmann M, Lin S and Lomax A 2005 Experimental characterization and physical modelling of the dose distribution of scanned proton pencil beams *Phys. Med. Biol.* **50** 541–61
Phillips M, Pedroni E, Blattmann H, Böhringer T, Coray A and Scheib S 1992 Effects of respiratory motion on dose uniformity with a charged particle scanning method *Phys. Med. Biol.* **37** 223–34
Riboldi M, Orecchia R and Baroni G 2012 Real-time tumour tracking in particle therapy: technological developments and future perspectives *Lancet Oncol.* **13** e383–91
Schätti A, Meer D and Lomax A 2014 First experimental results of motion mitigation by continuous line scanning of protons *Phys. Med. Biol.* **59** 5707–23
Schätti A, Zakova M, Meer D and Lomax A 2013 Experimental verification of motion mitigation of discrete proton spot scanning by re-scanning *Phys. Med. Biol.* **58** 8555–72
Seco J, Robertson D, Trofimov A and Paganetti H 2009 Breathing interplay effects during proton beam scanning: Simulation and statistical analysis *Phys. Med. Biol.* **54** N283–94

Smith A *et al* 2009 The M D Anderson proton therapy system *Med. Phys.* **36** 4068–83
Zenklusen S, Pedroni E and Meer D 2010 A study on repainting strategies for treating moderately moving targets with proton pencil beam scanning at the new Gantry 2 at PSI *Phys. Med. Biol.* **55** 5103–21
Zhang Y, Boye D, Tanner C, Lomax A and Knopf A 2012 Respiratory liver motion estimation and its effect on scanned proton beam therapy *Phys. Med. Biol.* **57** 1779–95
Zhang Y, Huth I, Wegner M, Weber D and Lomax A 2016 An evaluation of rescanning technique for liver tumour treatments using a commercial PBS proton therapy system *Radiother. Oncol.* **121** 281–7